Ultrasound in Medicine & Biology 51 (2025) 2039–2048

Contents lists available at ScienceDirect

Ultrasound in Medicine & Biology

journal homepage: www.elsevier.com/locate/ultrasmedbio

Original Contribution

Pulse-inversion Doppler-based Phase-compensation Reduces Decorrelation in High-frame Rate Contrast-enhanced Ultrasound

Hsin Huang [a,b], Yichuang Han [a], Hendrik J. Vos [a,c], Johan G. Bosch [a], Annemien van den Bosch [d], Antonius F.W. van der Steen [a,c], Chih-Chung Huang [b,e], Jason Voorneveld [a,f,*]

[a] Thorax Biomedical Engineering, Department of Cardiology, Erasmus MC University Medical Center, Rotterdam, the Netherlands
[b] Department of Biomedical Engineering, National Cheng Kung University, Tainan, Taiwan
[c] Department of Imaging Physics, Faculty of Applied Sciences, Delft University of Technology, Delft, the Netherlands
[d] Department of Cardiology, Erasmus MC University Medical Center, Rotterdam, the Netherlands
[e] Medical Device Innovation Center, National Cheng Kung University, Tainan, Taiwan
[f] BrainEcho Lab, Department of Neuroscience, Erasmus MC University Medical Center, Rotterdam, the Netherlands

ARTICLE INFO

Keywords:
High frame-rate imaging
Contrast-enhanced ultrasound
Decorrelation
Pulse-inversion Doppler
Phase compensation
Blood flow imaging
EchoPIV

ABSTRACT

Objective: High-frame-rate (HFR) ultrasonic imaging combined with an ultrasound contrast agent (UCA) can be used to study blood flow patterns using echo-particle image velocimetry (echoPIV). Pulse inversion is a common contrast-specific multipulsing scheme for suppressing tissue clutter in ultrasound images while selectively enhancing nonlinear signals from the UCA. However, in fast flow, the displacement of UCA between pulses leads to phase shifts in the echoes that may result in loss of UCA signal, hindering blood flow tracking with echoPIV.
Methods: In the present work, a phase-compensation algorithm is proposed to reduce motion-induced signal loss in HFR contrast-enhanced ultrasound imaging using pulse-inversion Doppler (PID).
Results: The PID-based phase-compensation algorithm increased image intensity in the high-velocity regions by up to 6 dB in both *in vitro* and patient data. Also, after PID-based phase compensation, echoPIV was able to measure 27% higher vector velocities in the patient data.
Conclusion: The results reveal the feasibility of PID-based phase compensation for reducing signal loss in fast-flow HFR contrast-enhanced ultrasound and its potential for improving blood flow estimation.

Introduction

High-frame-rate (HFR) contrast-enhanced ultrasound (CEUS), using ultrasound contrast agent (UCA) microbubbles, has become a useful tool for studying blood flow patterns, from microvascular flow in the brain [1], kidney [2,3], and myocardium [4–6] to macroscale flow in the abdominal aorta [7–10], femoral arteries [11,12], and the left ventricle (LV) [13,14]. With respect to the latter, HFR echo-particle image velocimetry (echoPIV) is a vector flow imaging technique particularly suited to LV blood flow imaging [14–19], where blood flow velocities in the LV (>1 m/s) necessitate frame rates in the kilohertz range to resolve the blood signal effectively.

To achieve rates of thousands of frames per second, diverging-wave transmission sequences are used, which encode the entire LV in a limited number of transmissions [20]. This comes at a cost of resolution, signal-to-noise ratio, and contrast, which can be offset by using multiangle coherent compounding [21,22]. Additionally, signal-to-noise ratio and blood-pool-to-tissue contrast can be improved further by using specialized CEUS sequences to suppress tissue signal while selectively retaining UCA signal in the blood [23–26].

Pulse inversion (PI) is one of the common contrast-specific multipulsing schemes for detecting flow in HFR CEUS [18,27,28]. PI consists of transmitting two consecutive alternating polarity pulses. The principle idea is that tissue clutter will scatter linearly, while the UCA will scatter nonlinearly (providing harmonics of the transmitted frequency). Thus, when the scattered signals from the two pulses are summed, the linear tissue signal cancels, while retaining the even-harmonic nonlinear UCA signals [24,26]. However, whenever the microbubbles move during the time interval between the two pulses, the second pulse gets an additional phase difference, causing an unwanted reduction of the nonlinear microbubble signal, manifesting as both reduced signal intensity and velocity magnitude underestimation after echoPIV analysis [15,17,19]. To explain why bubble motion between PI pulses results in velocity underestimation in echoPIV, it is useful to consider how color Doppler processing is affected by plane-wave angular compounding, which similarly assumes a linear superposition of scatterers between transmit–receive

* Corresponding author. BrainEcho Lab, Department of Neuroscience, Erasmus MC University Medical Center, 3015 GD, Rotterdam, the Netherlands.
E-mail address: j.voorneveld@erasmusmc.nl (J. Voorneveld).

https://doi.org/10.1016/j.ultrasmedbio.2025.07.017
Received 19 March 2025; Revised 19 June 2025; Accepted 15 July 2025

events. Ekroll et al. [29] showed that angular compounding of flowing blood signals causes both a loss of signal-to-noise ratio (intensity loss from out-of-phase summation) and a low-pass filtering effect on the velocity spectrum, biasing the measurement toward lower velocities. This same bias manifests itself in the temporal cross-correlation function used for displacement estimation in echoPIV.

Several methods have been proposed to compensate for motion in angular compounding: An echoPIV-specific method is to perform cross-correlation between the uncompounded images (per angle) and then sum the cross-correlation results from different angles [15,28,30]. However, these methods only avoid the decorrelation between angles and do not take advantage of the improved image quality after coherent compounding. Another approach to reduce decorrelation is to use motion or phase compensation. Denarie et al. [31] used cross-correlation to compensate for motion in rat hearts through coherent plane-wave compounding, in combination with using an altered ordering of the transmitted tilt angles, for example, switching the angles symmetrically around 0°: [−10°, 10°, −5°, 5°, 0°] instead of [−10°, −5°, 0°, 5°, 10°]. Porée et al. [32] demonstrated that human myocardial tissue motion artefacts could be compensated for by using slow-time lag-one autocorrelation, while also using an alternative sequence order. The two aforementioned studies were shown to compensate for the phase between different transmitting angles, but cannot directly process contrast-specific multipulsing sequences. Mougharbel et al. [33] further extended Porée's work to tissue harmonic imaging through PI. However, they only compensated for the phase between different transmitting angles for myocardium dynamics. Stanziola et al. [34] used a two-stage registration framework to compensate for the motion, but this strategy requires iterative optimization and would be difficult for real-time implementation. Recently, Lagrangian beamforming has also been proposed for improving myocardial vascular visibility. Still, its computational cost is high, because the delays in the delay-and-sum image reconstruction need to be updated every frame [35]. In summary, prior work still lacks an explicit approach for improving the phase coherence between the PI echoes of moving UCA and thus improving echoPIV accuracy in high-velocity flow applications.

In the present work, a phase-compensation algorithm is proposed to reduce motion-induced signal loss in HFR CEUS imaging. First, pulse-inversion Doppler (PID) is used to detect the phase shift of UCA between PI transmissions; then, the beam-formed in-phase/quadrature (IQ) data are motion compensated for using the measured PID phase shifts, allowing for coherent summation of the second-harmonic data. We compare the efficacy of both fundamental-frequency PID (1PID) and second harmonic PID (2HPID) as phase shift estimators. The phase-compensation accuracy was first evaluated *in vitro* in a straight tube flow phantom. *In vivo* capability was then demonstrated for LV flow in HFR CEUS patient data. The phase compensation effect on echoPIV tracking of high-velocity flows was also evaluated.

Theory

A typical PI series of K transmit pulses at a pulse repetition interval T can be expressed as [36]:

$$p_k(t) = (-1)^k p_0(t - kT),\ \ k\in[0,\ \ K-1]. \tag{1}$$

That is, each transmitted pulse is the inverse of the previous pulse. Each pulse is scattered by the UCA microbubbles in the field of view. Microbubbles scatter the ultrasound nonlinearly, resulting in received echoes that contain both odd and even harmonics of the originally transmitted pulses [36]. The odd harmonics (e_{odd}) (which includes the fundamental echo) and the even harmonics (e_{even}) (which includes the second harmonic echo) are related differently to those of the previous pulse,

$$Echo\{p(t)\} = e_{even}(t) + e_{odd}(t) \tag{2}$$

$$Echo\{-p(t)\} = e_{even}(t) - e_{odd}(t). \tag{3}$$

Equations 2 and 3 reveal that the odd harmonics changes sign owing to the inversion, whereas the even harmonics do not. Therefore, the phase shift of the odd harmonic ($\Delta\emptyset_{odd}$) gets an additional π term and that of the even harmonic ($\Delta\emptyset_{even}$) do not. This is written as

$$\Delta\emptyset_{odd} = 2\pi f_c \Delta\tau_d + \pi \tag{4}$$

$$\Delta\emptyset_{even} = 2\pi f_c \Delta\tau_d, \tag{5}$$

where f_c denotes the carrier frequency and $\Delta\tau_d$ is the time delay owing to the axial motion of scattering structure. Then, the estimated Doppler frequency of the odd-harmonic echoes ($f_{d,odd}$) and even-harmonic echoes ($f_{d,even}$) are:

$$f_{d,odd} = \frac{\Delta\emptyset_{odd}}{2\pi} f_{prf} = \frac{2v}{c} f_c + \frac{1}{2} f_{prf} \tag{6}$$

$$f_{d,even} = \frac{\Delta\emptyset_{even}}{2\pi} f_{prf} = \frac{2v}{c} f_c, \tag{7}$$

where f_{prf} is the pulse-repetition frequency ($\frac{1}{T}$), c is the speed of the sound, and v is the axial velocity ($v = \frac{c\Delta\tau_d}{2} f_{prf}$). That is, the Doppler frequency of the odd harmonic echoes will shift by $f_{prf}/2$ since the second pulse is inverted. Since the second harmonic (2H) nonlinear echoes appear around zero Hz in the Doppler spectrum, the 2H nonlinear echoes can be separated from the linear tissue scattering by using a low-pass filtering at cutoff frequency of pulse repetition frequency/4 [36–38]. Based on this theory, 1PID and 2HPID for detecting phase shifts between PI pulses were derived, as described in the following two subsections.

2HPID

Second harmonic data consist solely of even harmonic echoes. Modified from eqn 5, the 2H Doppler phase shift between PI pulses, $\emptyset_{2HPID}$ is:

$$\emptyset_{2HPID} = 2\pi f_{2H} \Delta\tau_d = \emptyset_{m2H}, \tag{8}$$

where f_{2H} is the 2H frequency; $\emptyset_{m2H}$ is the measured Doppler phase shift by using the lag-1 autocorrelation processing [39] on the 2H data. The axial velocity derived from the 2HPID will be:

$$v = \frac{cf_{prf}}{4\pi f_{2H}} \emptyset_{2HPID} = \frac{cf_{prf}}{4\pi f_{2H}} \emptyset_{m2H}. \tag{9}$$

1PID

Fundamental data are part of the odd-harmonic echoes. Modified from eqn 4, the fundamental Doppler phase shift between PI pulses $\emptyset_{1PID}$ is:

$$\emptyset_{1PID} = 2\pi f_1 \Delta\tau_d = \emptyset_{m\ 1} - \pi, \tag{10}$$

where f_1 is the fundamental frequency; $\emptyset_{m1}$ is the measured Doppler phase shift of the fundamental data. Assuming there is no aliasing, $\emptyset_{1PID}$ is in a range between $\pm\pi$ and, therefore, $\emptyset_{m1}$ should be in a range from 0 to 2π. However, the $\emptyset_{m1}$ is limited in a range between $\pm\pi$ owing to the inverse tangent operation in the autocorrelation method [39]. Therefore, $\emptyset_{m1}$ values in a range from $-\pi$ to 0 need to be shifted to a range from π to 2π as follows:

$$\emptyset_{m1}^{'} = \begin{cases} \emptyset_{m1} + 2\pi, & if\ \emptyset_{m1} < 0 \\ \emptyset_{m1}, & otherwise \end{cases}. \tag{11}$$

Then, eqn 10 is modified as:

$$\emptyset_{1PID} = 2\pi f_1 \Delta\tau_d = \emptyset_{m1}^{'} - \pi. \tag{12}$$

The axial velocity derived from the fundamental component will be:

$$v = \frac{cf_{prf}}{4\pi f_1} \emptyset_{1PID} = \frac{cf_{prf}}{4\pi f_1} \left(\emptyset_{m1}^{'} - \pi\right). \tag{13}$$

If axial velocities from 1PID and 2HPID are assumed identical, we get the relationship between $\emptyset_{1PID}$ and $\emptyset_{2HPID}$ by combining eqn 9 and eqn 13 (and using the definition in eqn 12):

$$\emptyset_{2HPID} = \frac{f_{2H}}{f_1}\emptyset_{1PID}. \tag{14}$$

Note that $f_{2H}/f_1 \neq 2$ in practice, owing to frequency-dependent attenuation that shifts the dominant frequency in ultrasound pulses to lower values with increasing depth.

Methods

Ultrasound acquisition sequence

A research ultrasound system (Vantage 256, Verasonics Inc., Kirkland, WA, USA) connected with a phased-array probe (P4-1, ATL) was used for the acquisition. The maximal imaging depth was limited to 12 cm. The voltage was 10 V and the mechanical index was less than 0.1 [18]. The HFR CEUS sequence consisted of a two alternating polarity pulses (PI, 1.5 MHz transmit, 2 cycle pulses), each transmitted with two angled (+7°, −7°) diverging waves (virtual focus = 47 mm). The pulse repetition frequency was set to 4900 Hz, resulting in an effective frame rate of 1225 Hz [18]. The saved RF data were passed through a fast-time fourth-order Butterworth bandpass filter around the 2H (2.6–3.8 MHz). Both unfiltered RF data and 2H-filtered RF data were beamformed with Verasonics' built-in beamformer on a 0.5 λ by 0.31° (axial, lateral) resolution grid to acquire fundamental and 2H beamformed data, respectively.

PI Doppler processing

Both fundamental and 2H data were filtered individually for each PI pulse and transmitting angle combination through a slow-time fourth-order Butterworth high-pass filter with a cutoff frequency of 100 Hz. Then, the filtered fundamental and 2H data were used for 1PID and 2HPID, respectively, to evaluate the fundamental and 2H phase shifts, which were then used, respectively, for compensating the clutter-filtered 2H data along the temporal domain. The window length for autocorrelation processing is 40 ms.

Phase compensation

Considering the transmitting scheme in this work (Fig. 1), the phase information of filtered 2H IQ data at negative-polarity transmitting pulse at transmitting angle 1 ($\angle x_{-,1}$) was considered as a reference point. Then, compensation was performed by adjusting the three other phase information [at positive-polarity, angle 1 ($\angle x_{+,1}$); at positive and negative polarity, angle 2 ($\angle x_{+,2}$ and $\angle x_{-,2}$, respectively)] as:

$$\angle x_{+,1}{}' = \angle x_{+,1} + \emptyset_{D,1} \tag{15}$$

$$\angle x_{+,2}{}' = \angle x_{+,2} - \emptyset_m \tag{16}$$

$$\angle x_{-,2}{}' = \angle x_{-,2} - (\emptyset_{D,2} + \emptyset_m), \tag{17}$$

where $\emptyset_m$ equals $(\emptyset_{D,1} + \emptyset_{D,2})/2$ and $\emptyset_{D,1}$ and $\emptyset_{D,2}$ indicate the phase shifts between PI pulses at two different transmitting angles, respectively.

Because the compensation was performed on filtered 2H data, $\emptyset_{D,1}$ and $\emptyset_{D,2}$ were directly derived from 2HPID. For instance, $\emptyset_{D,1}$ is:

$$\emptyset_{D,1} = \emptyset_{2HPID,1} = \frac{f_{2H}}{f_1}\emptyset_{1PID,1}, \tag{18}$$

where $\emptyset_{1PID,1}$ and $\emptyset_{2HPID,1}$ indicate the Doppler phase shifts from 1PID and 2HPID at transmitting angle 1, respectively. B-mode images were made by summing all transmit waves (pulses and angles) and envelope detection. The image intensity before and after phase compensation is calculated by taking the mean square amplitude in manually selected area. Images are shown with log-compression. All post-processing was performed in MATLAB (R2020b, MathWorks, Natick, MA, USA).

Experiments

In vitro flow phantom experiment

A Doppler flow phantom (ATS model 524, CIRS Inc., Norfolk, VA, USA) was connected to a peristaltic pump (Verder Liquids, Utrecht, the Netherlands) for *in vitro* phantom experiments. The tube diameter of the flow phantom was 8 mm. The maximal flow velocity was set to approximately 1 m/s, which was confirmed by spectral Doppler through a commercial ultrasound system (Zonare ZS3, Mindray, Shenzhen, China). An UCA (SonoVue, Bracco Imaging, SpA, Milano, Italy) solution

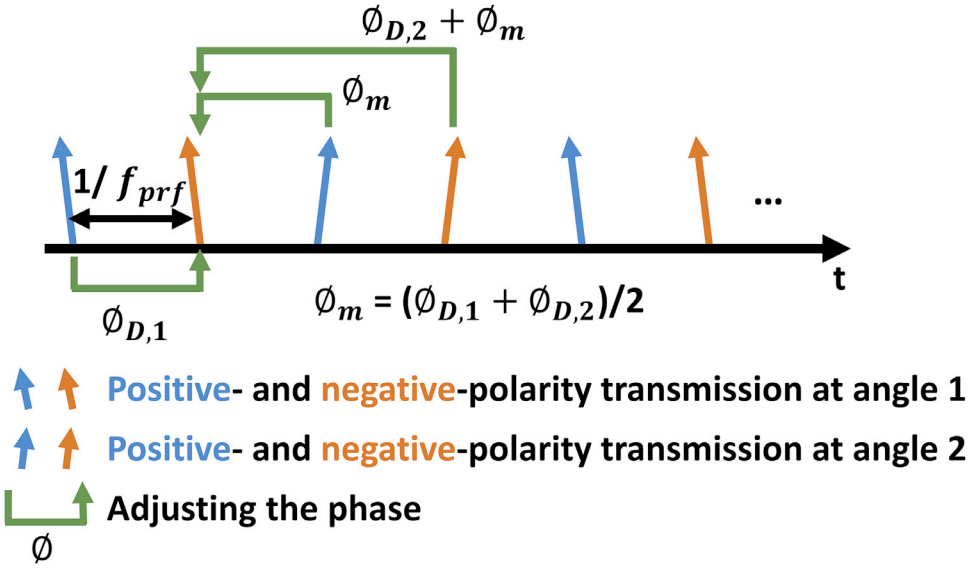

Figure 1. The diagram of the pulse-inversion sequence and phase-compensation. $\emptyset_{D,1}$ and $\emptyset_{D,2}$. the phase shifts between PI pulses at transmission angles 1 and 2, respectively.

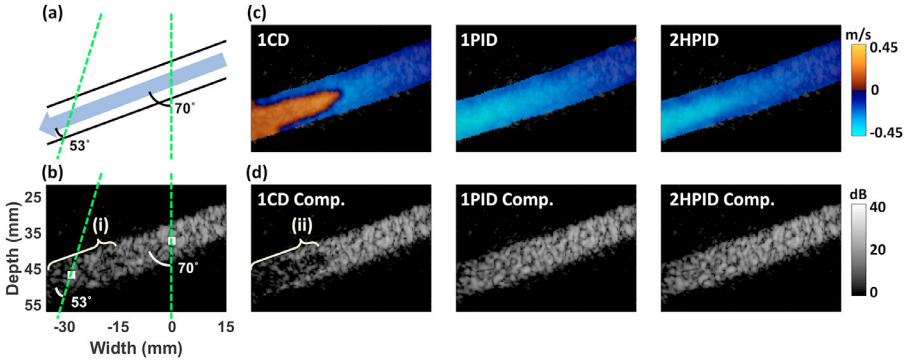

Figure 2. Flow phantom images. (a) Diagram of the flow phantom setup with beam-to-flow angles of 53° and 70°. (b) Flow phantom HFR CEUS B-mode image with no compensation. (c) Axial velocity images from 1CD, 1PID, and 2HPID and (d) the B-mode images after 1CD-, 1PID-, and 2HPID-based phase-compensation (Comp.). (i) and (ii) indicate the original decorrelation region and the decorrelation region after 1CD-based phase compensation, respectively. 1CD, fundamental-mode color Doppler; 1PID, fundamental-mode pulse-inversion Doppler; 2HPID, second-harmonic pulse inversion Doppler; CEUS, contrast-enhanced ultrasound; HFR, high-frame-rate.

(concentration: ~45 μL/L) was used. For HFR CEUS acquisition, the transducer was inclined at 20°. Regions of 2 mm × 2 mm (Fig. 2b) were selected for quantitative analysis of image intensity. Five pump cycles were analyzed independently and used as samples for a paired samples *t* test, with statistical significance defined as a *p* value of less than 0.05 for differences between methods.

In vivo *human experiment*

The method was tested on data acquired previously [18] *in vivo* for echoPIV on patients presenting with heart failure (protocol approved by the Institutional Review Board of the Erasmus MC - NL63755.078.18).

The LV apical view of patients was imaged after intravenous injection of a diluted solution of UCA (5 mL SonoVue in 15 mL isotonic saline) using a continuous infusion pump (1.2 mL/min, VueJect BR-INF 100, Bracco Imaging, SpA, Milan, Italy) connected to the recommended infusion kit [9]. After confirming the arrival of UCA in the LV, HFR CEUS imaging was performed for approximately 2.5 seconds. Regions of 4 mm × 4 mm were selected for quantitative analysis of intensity and axial velocity between processing methods. B-mode intensities in fast-flow regions (mitral inflow jet, aortic outflow tract) were compared before and after phase compensation. The difference in intensity is reported in decibels as measured over 124 frames (~0.1 s).

Data analysis

Color Doppler comparison

In addition to 1PID and 2HPID, conventional fundamental color Doppler (1CD) processing was added to the comparison in the *in vitro* flow phantom experiment, which was independently calculated for each PI pulse and transmitting angle. Because 1CD measures the phase shift between pulses at same polarity and same angle, 1CD phase shifts were divided by number of angle ($NA = 2$ in this work) and PI factor ($PI_{factor} = 2$). Then phase shifts for the same transmitting angle but for different polarities were averaged. That is, eqn 18 is adopted for CD by

$$\emptyset_{D,1} = \emptyset_{2HPID,1} = \frac{f_{2H}}{f_1}\emptyset_{1PID,1} = \frac{f_{2H}}{f_1}\frac{\left(\emptyset_{1CD+,1} + \emptyset_{1CD-,1}\right)}{2{\cdot}NA{\cdot}PI_{factor}}, \quad (19)$$

where $\emptyset_{1CD+,1}$ and $\emptyset_{1CD-,1}$ indicate Doppler phase shifts from 1CD in positive- and negative-polarity pulses at transmitting angle 1, respectively.

EchoPIV

EchoPIV subdivides the envelope-detected image into small, equally sized, overlapping blocks. Then, a normalized cross-correlation is computed for a search region around each block and the displacement per block between the two frames is obtained by locating the correlation peak of each search region. A more detailed description is provided in our previous work [18,19]. The final frame rate (after compounding and ensemble averaging) of the velocity data was 122 Hz. EchoPIV maximum velocity magnitudes in fast-flow regions (mitral inflow jet, aortic outflow tract) were compared before and after phase compensation.

Results

In vitro

Figure 2a shows a diagram of the flow phantom setup with flow direction and the effective beam-to-flow angles in the two measurement regions studied in Figure 3. The pulsed-wave Doppler imaging from the clinical Zonare ZS3 system, confirming a peak velocity of approximately 1 m/s, is shown in Supplementary Figure S1. In Figure 2b, a lower B-mode intensity can be observed in the lower left corner (beam-to-flow angle = 53°) than in the center (beam-to-flow angle = 70°). This is due to loss of phase coherence from the higher axial flow velocity in the lower-left corner (Fig. 2c). Aliasing was observed in the lower-left corner of the 1CD image owing to its insufficient Nyquist velocity (0.286 m/s). In contrast, because the Nyquist velocities of 1PID and 2HPID depend on f_{prf} (4900 Hz), the Nyquist velocities are higher (1.144 m/s and 0.596 m/s, respectively) in these modes. The motion-compensated images are shown in Figure 2d, based on phase shift estimates from 1CD, 1PID, and 2HPID. Owing to the aliasing problem, the decorrelation in the lower left corner became even more severe in the 1CD-compensated image (i vs. ii regions in Fig. 2). The phase incoherence in both 1PID- and 2HPID-compensated images, in contrast, was decreased successfully, as confirmed by the increase in B-mode intensity near the lower left corner, compared with the image without compensation (Fig. 2b).

Quantitatively, aliasing was evident in the 1CD velocity profile (blue dashed line), whereas both 1PID (yellow dashed–dotted line) and 2HPID (purple solid line) velocity profiles were close to reaching the expected peak velocity (−0.5 m/s). The aliasing in 1CD had the effect of further B-mode intensity deterioration after compensation (−3.3 ± 0.4 dB compared with the uncompensated image, $p < 0.001$). Conversely, the 1PID- and 2HPID-based compensation resulted in reduced decorrelation and increased time-averaged intensities compared with the uncompensated image (Fig. 3b; 6.1 ± 0.1 dB [1PID] and 6.3 ± 0.2 dB [2HPID]; both $p < 0.001$). Figures 3 (c and d) demonstrate the velocity and intensity profiles in the central area, with beam-to-flow angle of 70°. The maximum axial velocity in this area was 0.225 m/s. Therefore, no aliasing was observed in this area (Fig. 3c) and the intensity profiles after 1CD-, 1PID-, and 2HPID-based compensation were nearly identical (Fig. 3d; improvements of 3.3 ± 0.4 dB [1CD], 3.3 ± 0.4 dB [1PID], and 3.3 ± 0.4 dB [2HPID]; all $p < 0.001$).

In vivo

Figure 4a demonstrates an example apical three-chamber left ventricular B-mode image without compensation in a patient during ventricular filling (t = 0.28 s). The phase incoherence upon motion is distinguished by a relatively lower B-mode intensity (white-dashed region in Fig. 4a), was observed near the ventricular inflow region. This faster velocity caused considerable aliasing in the 1CD image (green-dashed regions in Fig. 4b), and hence significant decorrelation in the

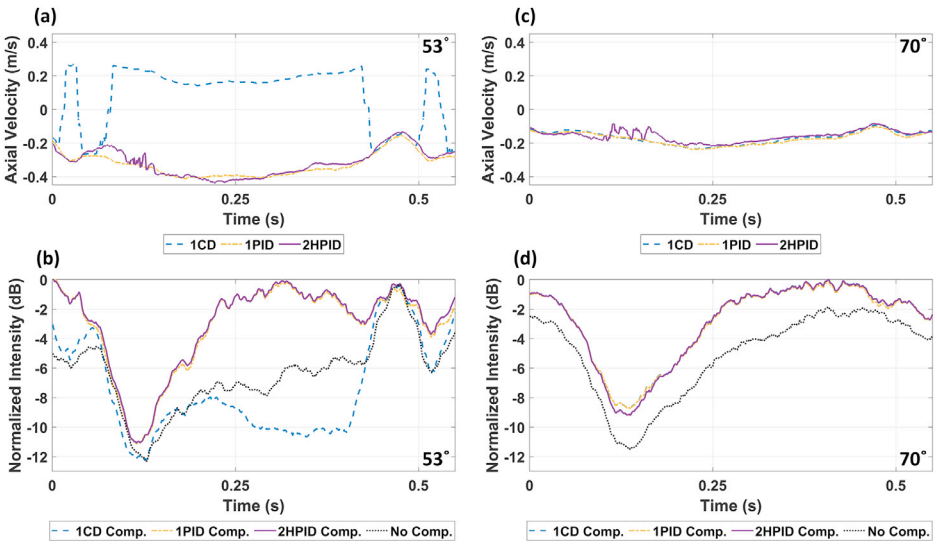

Figure 3. Quantitative comparisons of axial velocities and B-mode intensities. (a) Average axial flow velocities and (b) B-mode intensities in 53° beam-to-flow angle region. (c) Average axial flow velocities and (d) B-mode intensities in the 70° beam-to-flow angle region. 1CD, fundamental-mode color Doppler; 1PID, fundamental-mode pulse-inversion Doppler, 2HPID, second-harmonic pulse inversion Doppler; Comp., compensation.

1CD-compensated image (green-dashed regions in Fig. 4d). In contrast, there was no aliasing in the 2HPID image (Fig. 4c), and decorrelation was reduced in the 2HPID-compensated image (Fig. 4e). Similarly, during ventricular ejection (t = 0.71 s), decorrelation (white-dashed region in Fig. 5a) was observed near the ventricular outflow tract. Aliasing was again observed in the 1CD image and decorrelation was not reduced (green-dashed regions in Fig. 5 [b and d]). While after 2HPID-based compensation, the decorrelation in the outflow region was significantly improved (Fig. 5e). Supplementary Figure S2 shows the spectral Doppler from fundamental data in both the inflow and outflow regions to illustrate the aliasing. After 2HPID-based compensation, echoPIV was able to measure higher vector velocities (Figs. 4 [f and h]; Figs. 5 [f and h]). In contrast, echoPIV after 1CD-based compensation seemed to underestimate the vector velocities compared with the uncompensated echoPIV (Figs. 4 [f and g]; Figs. 5 [f and g]).

During early filling (0.2–0.3 s; grey region in Fig. 6d) the time-averaged intensity (in the inflow region; Fig. 6a – magenta) of the 2HPID-compensated image increased by 4.7 ± 1.5 dB compared with the uncompensated image (Fig. 6d). However, after 1CD-based compensation, the time-averaged intensity increased by only 1.2 ± 1.3 dB (Fig. 6d), owing to aliasing in part of the inflow region (Fig. 4b). During ejection (0.7–0.8 s; grey region in Fig. 6e), time-averaged intensity (in the outflow region; Fig. 6a, green) of the 2HPID-compensated image increased by 5.7 ± 1.4 dB compared with the uncompensated image (Fig. 6e). For the 1CD-compensated image, the decorrelation worsened, with time-averaged intensity decrease by 2.9 ± 1.5 dB compared with the uncompensated image (Fig. 6e), also owing to aliasing in the outflow region (Figs. 5 [b, d]). The corresponding comparison of axial velocities between 1CD and 2HPID in the inflow and outflow windows over time confirms the aliasing issue (Figs. 6 [b, c]). After 2HPID-based

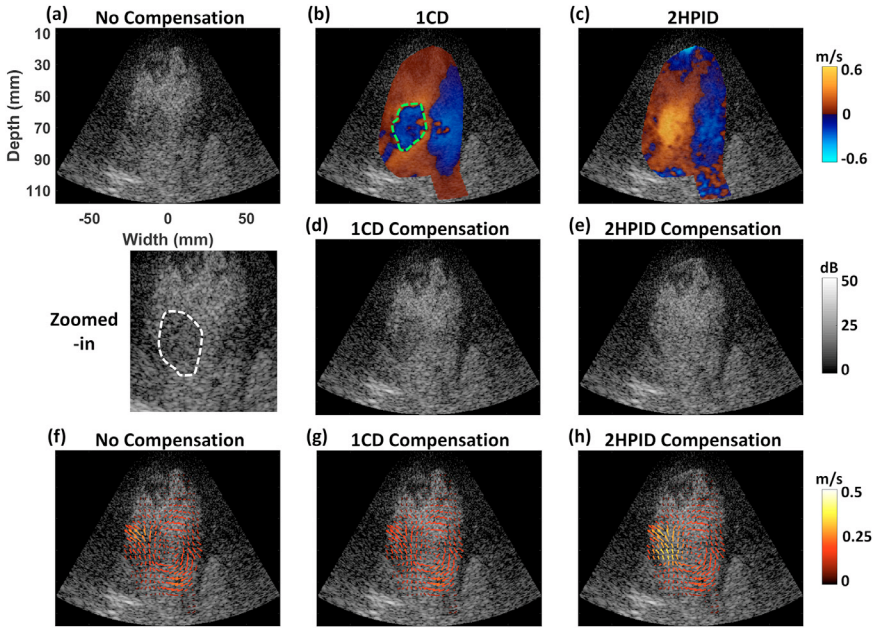

Figure 4. Example apical three-chamber left ventricular images in patient 1 during ventricular filling (t = 0.28 s). (a) HFR CEUS B-mode image with no compensation and its zoomed-in image. (b) Axial velocity images from 1CD and (c) 2HPID. B-mode images after (d) 1CD- and (e) 2HPID-based phase compensation. EchoPIV images before (f) and after (g) 1CD- and (h) 2HPID-based compensation. *White and green dashed windows* indicate the original decorrelation region and aliasing region, respectively. 1CD, fundamental-mode color Doppler; 2HPID, second-harmonic pulse inversion Doppler; CEUS, contrast-enhanced ultrasound; HFR, high-frame-rate.

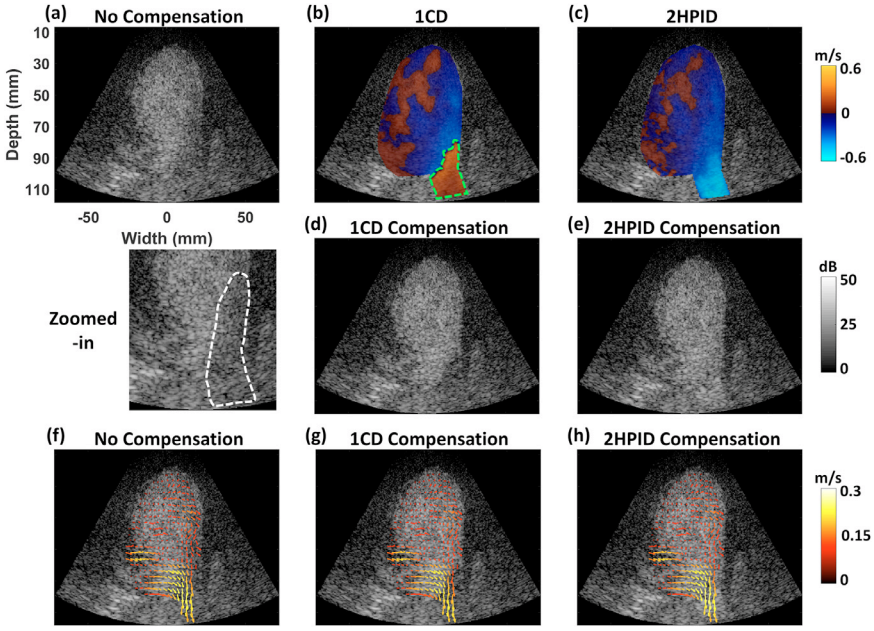

Figure 5. Example apical three-chamber left-ventricular images in patient 1 during ventricular ejection (t = 0.71 s). (a) HFR CEUS B-mode image with no compensation and its zoomed-in image. (b) Axial velocity images from 1CD and (c) 2HPID; B-mode images after (d) 1CD- and (e) 2HPID-based phase compensation. EchoPIV images before (f) and after (g) 1CD- and (h) 2HPID-based compensation. *White and green dashed windows* indicate the original decorrelation region and aliasing region, respectively. 1CD, fundamental-mode color Doppler, and 2HPID, second-harmonic pulse inversion Doppler; CEUS, contrast-enhanced ultrasound; HFR, high-frame-rate.

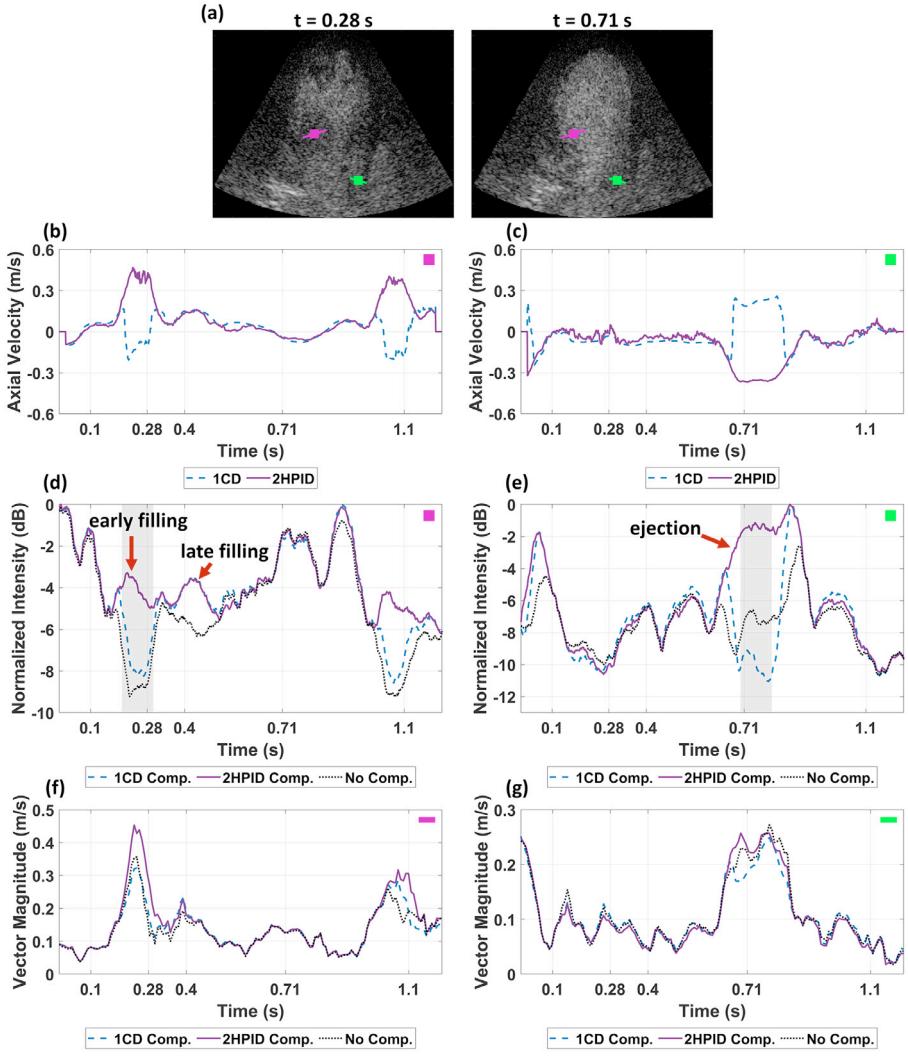

Figure 6. Quantitative comparisons. (a) Position of selected inflow (*magenta-boxed window and section*) and outflow (*green-boxed window and section*) areas. (b and c) Axial velocities in the inflow (b) and outflow (c) windows over time. (d and e) Average B-mode intensities in the inflow (d) and outflow (e) windows over time before and after phase compensation. (f and g) echoPIV-derived vector velocity magnitudes in the inflow and outflow sections. 1CD, fundamental-mode color Doppler; 2HPID, second-harmonic pulse inversion Doppler; Comp., compensation.

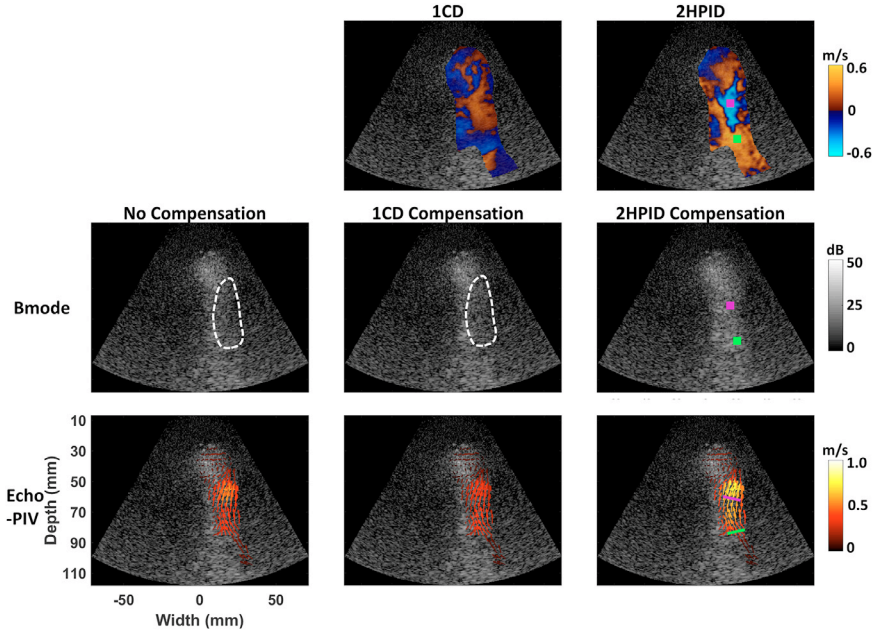

Figure 7. Example ventricular images in patient 2. Axial velocity images from 1CD and 2HPID (*top*). HFR CEUS B-mode images (*center*) and echoPIV images (*bottom*) before and after 1CD- and 2HPID-based compensation. The *magenta* (aliasing) and *green* (nonaliasing) boxes indicate the areas for B-mode intensities comparisons. Similarly, the *magenta and green lines* indicate the areas for vector velocities magnitude comparisons. *White dashed windows* indicate the decorrelation region. 1CD, fundamental-mode color Doppler; 2HPID, second-harmonic pulse inversion Doppler; CEUS, contrast-enhanced ultrasound; HFR, high-frame-rate.

compensation, the vector magnitude from echoPIV increased by 27% and 12% in the inflow and outflow regions, respectively (Figs. 6 [g, f]).

Figure 7 demonstrates another example in a patient with constrictive pericarditis resulting in higher velocity magnitudes in the LV. Notably, in this case, aliasing occurred in 2HPID image but the image intensity values were still recovered after compensation (Fig. 8a). This is because, theoretically, the aliasing in 2HPID is not as critical for phase-compensation between PI pulses (as compared with CD; see Appendix). Comparing regions with and without aliasing in 2HPID (Figs. 8 [a and c], respectively), we see that time-averaged intensity was increased by 4.1 ± 1.3 dB and 2.9 ± 1.5 dB compared with the uncompensated image over the filling period (0.25–0.35 s, grey region in Figs. 8 [a and c]). After converting the same two regions into cross-sections (Fig. 7, bottom right tile) the vector velocity magnitudes could be compared (Figs. 8 [b and d]), revealing an increase in velocity magnitude of 16% and 20% in the aliasing-free and aliased areas, respectively.

Discussion

In the present study, PID-based phase compensation was proposed for reducing the phase incoherence between received PI signals. First, to ensure feasibility, we tested the capability of two proposed PID methods in a phantom study. After performing phase compensation based on PID phase shifts, it was clear that the coherence was significantly restored, as the intensity increased by up to 6 dB (Fig. 2d and Fig 3b). This phantom work demonstrated the feasibility of the PID-based compensation methods, but was limited because of the stable flow in the phantom, with minimal tissue movement or vibration.

The feasibility of the proposed method was further demonstrated with patient data (Figs. 4-6). As expected, aliasing occurred in CD images owing to the Nyquist velocity limits and a decorrelation remains in 1CD-compensated images, whereas the phase coherence after PID-based compensation was increased. We also investigated the

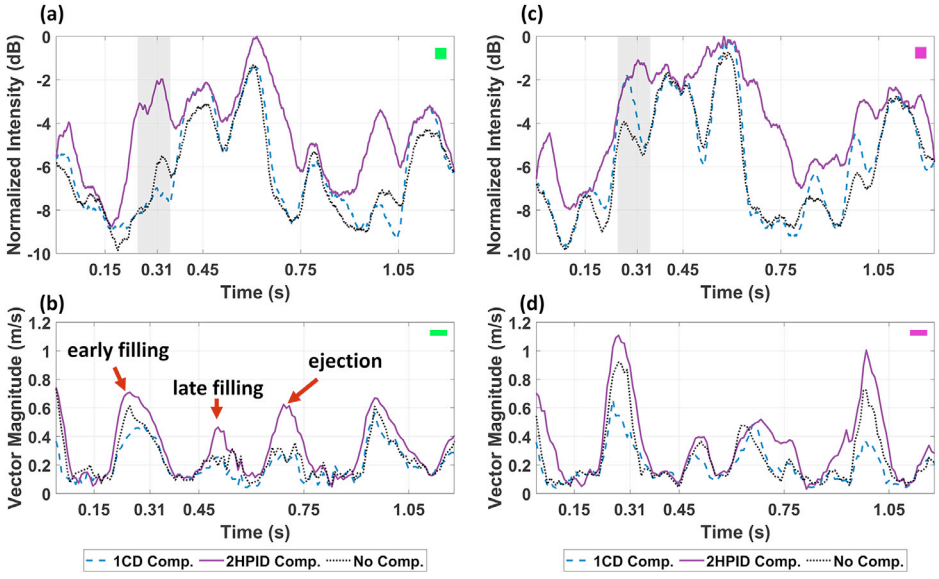

Figure 8. Quantitative comparisons of B-mode intensities and vector velocities magnitude for patient 2. (a) Average B-mode intensities and (b) average vector velocity magnitude in the aliasing-free area. (c) Average B-mode intensities and (d) average vector velocity magnitude in the aliasing area. The selected areas and sections are labeled in Figure 7. 1CD, fundamental-mode color Doppler, and 2HPID, second-harmonic pulse inversion Doppler; Comp., compensation.

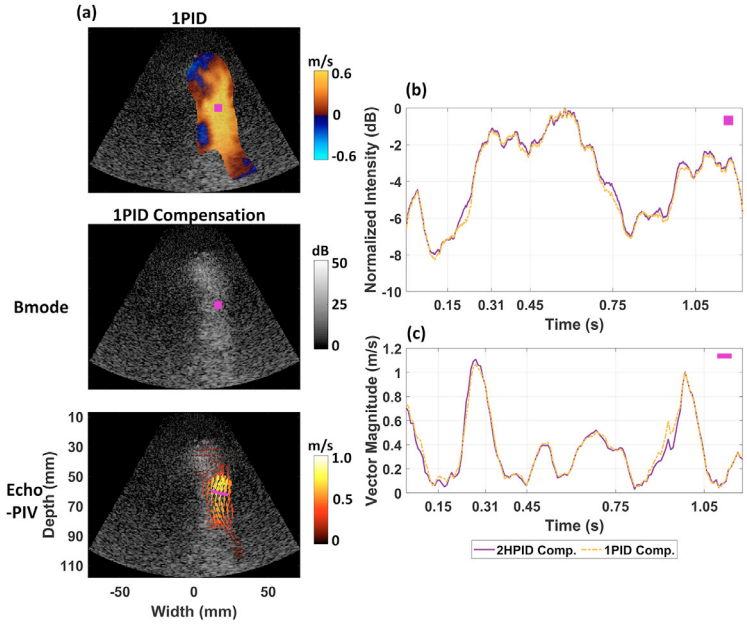

Appendix Figure 1. (a) 1PID-compensated B-mode and echoPIV after 1PID-based compensation in patient 2. (b) Quantitative comparisons of B-mode intensities and (c) vector velocities magnitude between 1PID and 2HPID methods. 1PID, fundamental-mode pulse-inversion Doppler, and 2HPID, second-harmonic pulse inversion Doppler; Comp., compensation

performance of the proposed methods on another set of patient data with both lower image quality and higher filling velocities (Figs. 7 and 8). It was demonstrated that, even though the imaging quality was less than ideal, and aliasing occurred in the 2HPID data, the decorrelation could still be reduced considerably. This is because the proposed PID directly measures the phase shifts between the PI echoes, whereas conventional 1CD measures the phase shifts between frames. Therefore, the phase shifts detected by 1CD must be divided by the number of transmit angles and the PI factor for compensating the PI pulses (eqn 19). However, owing to this division operation, it becomes necessary to know the aliasing folding number of the 1CD (Appendix and App. Fig. 1). Finally, we investigated how compensating phase shifts affect echoPIV (Figs. 7 and 8). It was observed that after compensation, echoPIV was able to measure higher vector velocities. They increased by 27% and 12% in the inflow and outflow regions in patient 1, and by 16% and 20% in magnitude in aliasing-free and aliasing areas in patient 2, respectively.

In [31] and [32], tissue motion was corrected through cross-correlation [31] or a Doppler method [32] to detect phase information between different angles. Because we are compensating for blood flow, which moves at a much higher velocity than tissue, aliasing is likely. Aliasing in phase shifts between different angles makes it difficult to interpolate the phase shift required to compensate between PI pulses. In [33], the concept of harmonic Doppler estimation is similar to our 2HPID, but it was applied for cardiac tissue harmonic imaging, not CEUS imaging. Additionally, they mentioned that their compensation was limited by the Nyquist velocity; while we found that the Nyquist limitation in PID did not affect the results of compensation (Figs. 7 and 8; Appendix; Supplementary Fig. S1). The imaging registration method [34] or Lagrangian method [35] has the potential to reduce the decorrelation. However, both of these methods inherently involve a relatively large computational burden. PID has the potential for real-time compensation, owing to its low computational complexity.

Still, there are some remaining challenges and limitations that should be noted. First, for fair comparison the same slow-time filter was used for both 1CD and PID. However, PID images were slightly noisier compared with 1CD images, which may imply this filter was not optimal for PID. We have also tried a polynomial regression filter [40], although we did not observe a significant improvement. Second, 1PID is able to measure a higher axial velocity than 2HPID. Yet, for phase compensation, its phase shifts need to be multiplied by $\frac{f_{2H}}{f_1}$ because 2H data were being compensated in this study. f_1 and f_{2H} were evaluated by using the fast Fourier transform along the fast-time domain. Yet, this approach essentially assumes that the frequency distribution is constant over depth. Although this assumption may be valid in stable flow phantoms, it can introduce errors *in vivo* owing to significant variations in ventricular flow. A 2D autocorrelator [41] may be a promising solution for optimizing the estimation of f_1 andf_{2H}. Finally, after improving the phase coherence by the proposed PID-based compensation, it was observed that echoPIV was able to capture higher vector velocities. These higher vector velocities were not validated against a ground truth, because that was not available.

Conclusions

A PID-based phase-compensation method was developed and validated in this work for the reduction of motion-induced phase incoherence in HFR CEUS imaging. A flow phantom study demonstrated the feasibility of the proposed method, while the application on two *in vivo* datasets further showcased its capabilities. It also revealed that after the proposed compensation, echoPIV showed greater velocity magnitudes.

Conflict of interest

The authors declare no competing interests.

Data Availability Statement

The authors declare that the data that support the finding of this study are available within the paper and its appendix data. The datasets are available from the corresponding author upon reasonable request.

Acknowledgments

This research was supported by National Science and Technology Council (NSTC), Taiwan, under the Dragon Gate Program (Grand No.: NSTC 112-2926-I-006-508-G).

Supplementary materials

Supplementary material associated with this article can be found in the online version at doi:10.1016/j.ultrasmedbio.2025.07.017.

APPENDIX

The relationship between the exact Doppler phase shift between PI pulses $\emptyset_D$ and the phase shift detected by PID is expressed as:

$$\emptyset_D = \emptyset_{PID} + 2n_{PID}\pi, \tag{20}$$

where n_{PID} is an integer aliasing folding number in PID. When aliasing does not occur, n_{PID} equals 0. Modifying from eqn 15, using the exact Doppler phase shift to compensate the phase information of IQ data at positive-polarity pulse $\angle x_+$ is:

$$\angle x_{+,D} = \angle x_+ + \emptyset_{D.} \tag{21}$$

Then, using phase shift detected by PID for compensation, is:

$$\angle x_{+,PID} = \angle x_+ + \emptyset_{PID} = \angle x_+ + (\emptyset_D - 2n_{PID}\pi). \tag{22}$$

Therefore, the phase difference between $\angle x_{+,D}$ and $\angle x_{+,PID}$ is $2n_{PID}\pi$. Since this difference is an integer multiple of 2π, $\angle x_{+,D}$ and $\angle x_{+,PID}$ are equivalent for IQ data. That is, for phase-compensation, whether aliasing occurs in the PID does not affect the final phase compensation result. In contrast, because conventional CD detects the phase shift between same polarity and angle, the phase shift detected by CD, $\emptyset_{CD}$, must be divided by number of angles ($NA = 2$) and PI factor ($PI_{factor} = 2$) for compensating the phase shift between PI pulse as:

$$\angle x_{+,CD} = \angle x_+ + = \angle x_+ + \frac{\emptyset_D - 2n_{CD}\pi}{NA*}, \tag{23}$$

where n_{CD} is an integer aliasing folding number in CD. Therefore, the phase difference between $\angle x_{+,D}$ and $\angle x_{+,CD}$ will not always be an integer multiple of 2π owing to the division. In other words, for CD-based compensation, it becomes necessary to know the exact n_{CD}.

Supplementary Figure 1 demonstrates ventricular 1PID images from the same patient as Figs. 7-8. Owing to the higher Nyquist velocity in 1PID, aliasing didn't occur. It can be observed that the B-mode and echoPIV images after 1PID-based compensation (App. Fig. 1a) were similar to those after 2HPID-based compensation (Fig. 7). Appendix Figs. 1b and further compare B-mode intensity and vector velocity magnitude from echoPIV, respectively, in the selected aliasing areas (indicated in App. Fig. 1a). Both the intensity profiles and vector velocity magnitude profiles are almost overlapping between the 1PID and 2HPID methods. This example demonstrates that aliasing in PID does not affect the phase compensation for PI pulses.

References

[1] Errico C, Pierre J, Pezet S, Desailly Y, Lenkei Z, Couture O, et al. Ultrafast ultrasound localization microscopy for deep super-resolution vascular imaging. Nature 2015;527:499–502.

[2] Andersen SB, Taghavi I, Kjer HM, Søgaard SB, Gundlach C, Dahl VA, et al. Evaluation of 2D super-resolution ultrasound imaging of the rat renal vasculature using ex vivo micro-computed tomography. Sci Rep 2021;11:24335.

[3] Wei L, Wahyulaksana G, Te Lintel Hekkert M, Beurskens R, Boni E, Ramalli A, et al. High-frame-rate volumetric porcine renal vasculature imaging. Ultrasound Med Biol 2023;49:2476–82.

[4] Maresca D, Correia M, Villemain O, Bizé A, Sambin L, Tanter M, Ghaleb B, et al. Non-invasive imaging of the coronary vasculature using ultrafast ultrasound. JACC Cardiovasc Imaging 2018;11:798–808.

[5] Wahyulaksana G, Wei L, Voorneveld J, Hekkert MTL, Strachinaru M, Duncker DJ, et al. Higher-order singular value decomposition filter for contrast echocardiography. IEEE Trans Ultrason Ferroelectr Freq Control 2023;70:1371–83.

[6] Yan J, Huang B, Tonko J, Toulemonde M, Hansen-Shearer J, Tan Q, et al. Transthoracic ultrasound localization microscopy of myocardial vasculature in patients. Nat Biomed Eng 2024;8:689–700.

[7] Engelhard S, Voorneveld J, Vos HJ, Westenberg JJM, Gijsen FJH, Taimr P, et al. High-frame-rate contrast-enhanced US particle image velocimetry in the abdominal aorta: first human results. Radiology 2018;289:119–25.

[8] Voorneveld J, Engelhard S, Vos HJ, Reijnen MMPJ, Gijsen F, Versluis M, et al. High-frame-rate contrast-enhanced ultrasound for velocimetry in the human abdominal aorta. IEEE Trans Ultrason Ferroelectr Freq Control 2018;65:2245–54.

[9] Engelhard S, van Helvert M, Voorneveld J, Bosch JG, Lajoinie GPR, Versluis M, et al. US velocimetry in participants with aortoiliac occlusive disease. Radiology 2021;301:332–8.

[10] Engelhard S, van Helvert M, Voorneveld J, Bosch JG, Lajoinie G, Jebbink EG, et al. Blood flow quantification with high-frame-rate, contrast-enhanced ultrasound velocimetry in stented aortoiliac arteries: *in vivo* feasibility. Ultrasound Med Biol 2022;48:1518–27.

[11] van Helvert M, Engelhard S, Voorneveld J, van der Vee M, Bosch JG, Versluis M, et al. High-frame-rate contrast-enhanced ultrasound particle image velocimetry in patients with a stented superficial femoral artery: a feasibility study. Eur Radiol Exp 2022;6:32.

[12] van de Velde L, van Helvert M, Engelhard S, Ghanbarzadeh-Dagheyan A, Mirgolbabaee H, Voorneveld J, et al. Validation of ultrasound velocimetry and computational fluid dynamics for flow assessment in femoral artery stenotic disease. J Med Imaging 2024;11:037001.

[13] Toulemonde MEG, Corbett R, Papadopoulou V, Chahal N, Li Y, Leow CH, et al. High frame-rate contrast echocardiography: in-human demonstration. JACC Cardiovasc Imaging 2018;11:923–4.

[14] Strachinaru M, Voorneveld J, Keijzer LBH, Bowen DJ, Mutluer FO, Cate FT, et al. Left ventricular high frame rate echo-particle image velocimetry: feasibility and comparison with conventional echocardiography. Eur Heart J Cardiovasc Imaging 2022;23 (Suppl 1) jeab289-001.

[15] Voorneveld J, Muralidharan A, Hope T, Vos HJ, Kruizinga P, van der Steen AFW, Gijsen FJH, et al. High frame rate ultrasound particle image velocimetry for estimating high velocity flow patterns in the left ventricle. IEEE Trans Ultrason Ferroelectr Freq Control 2018;65:2222–32.

[16] Voorneveld J, Keijzer LBH, Strachinaru M, Bowen DJ, Goei JSL, Ten Cate F, et al. High-frame-rate echo-particle image velocimetry can measure the high-velocity diastolic flow patterns. Circ Cardiovasc Imaging 2019;12:e008856.

[17] Vos HJ, Voorneveld JD, Groot Jebbink E, Leow CH, Nie L, van den Bosch AE, et al. Contrast-enhanced high-frame-rate ultrasound imaging of flow patterns in cardiac chambers and deep vessels. Ultrasound Med Biol 2020;46:2875890.

[18] Voorneveld J, Keijzer LBH, Strachinaru M, Bowen DJ, Mutluer FO, van der Steen AFW, et al. Optimization of microbubble concentration and acoustic pressure for left ventricular high-frame-rate EchoPIV in patients. IEEE Trans Ultrason Ferroelectr Freq Control 2021;68:2432–43.

[19] Han Y, Bowen DJ, Barreto BL, Zwaan RR, Strachinaru M, van der Geest RJ, et al. Validation of left ventricular high frame rate echo-particle image velocimetry against 4D flow MRI in patients. Ultrasound Med Biol 2025;51:94–101.

[20] Tanter M, Fink M. Ultrafast imaging in biomedical ultrasound. IEEE Trans Ultrason Ferroelectr Freq Control 2014;61:102–19.

[21] Montaldo G, Tanter M, Bercoff J, Benech N, Fink M. Coherent plane-wave compounding for very high frame rate ultrasonography and transient elastography. IEEE Trans Ultrason Ferroelectr Freq Control 2009;56:489–506.

[22] Papadacci C, Pernot M, Couade M, Fink M, Tanter M. High-contrast ultrafast imaging of the heart. IEEE Trans Ultrason Ferroelectr Freq Control 2014;61:288–301.

[23] Burns PN, Wilson SR, Simpson DH. Pulse inversion imaging of liver blood flow: improved method for characterizing focal masses with microbubble contrast. Invest Radiol 2000;35:58.

[24] Whittingham TA. Contrast-specific imaging techniques: technical perspective. Contrast media in ultrasonography: basic principles and clinical applications. Berlin, Heidelberg: Springer Berlin Heidelberg; 2005. p. 43–70.

[25] Eckersley RJ, Chin CT, Burns PN. Optimising phase and amplitude modulation schemes for imaging microbubble contrast agents at low acoustic power. Ultrasound Med Biol 2005;31:213–9.

[26] Averkiou MA, Bruce MF, Powers JE, Sheeran PS, Burns PN. Imaging methods for ultrasound contrast agents. Ultrasound Med Biol 2020;46:498–517.

[27] Toulemonde M, Li Y, Lin S, Cordonnier F, Butler M, Duncan WC, et al. High-frame-rate contrast echocardiography using diverging waves: Initial in vitro and in vivo evaluation. IEEE Trans Ultrason Ferroelectr Freq Control 2018;65:2212–21.

[28] Leow CH, Tang MX. Spatio-temporal flow and wall shear stress mapping based on incoherent ensemble-correlation of ultrafast contrast enhanced ultrasound images. Ultrasound Med Biol 2018;44:134–52.

[29] Ekroll IK, Voormolen MM, K-V. Standal O, Rau JM, Lovstakken L. "Coherent Compounding in Doppler Imaging. IEEE Trans Ultrason Ferroelectr Freq Control 2015;65:1634–43.

[30] Leow CH, Bazigou E, Eckersley RJ, Yu ACH, Weinberg PD, Tang MX. Flow velocity mapping using contrast enhanced high-frame-rate plane wave ultrasound and image tracking: Methods and initial in vitro and in vivo evaluation. Ultrasound Med Biol 2015;41:2913–25.

[31] Denarie B, Tangen TA, Ekroll IK, Rolim N, Torp H, Bjåstad T, et al. Coherent plane wave compounding for very high frame rate ultrasonography of rapidly moving targets. IEEE Trans Med Imaging 2013;32:1265–76.

[32] Poree J, Posada D, Hodzic A, Tournoux F, Cloutier G, Garcia D. High-frame-rate echocardiography using coherent compounding with Doppler-based motion-compensation. IEEE Trans Med Imaging 2016;35:1647–57.

[33] Mougharbel M, Poree J, Posada D, Hodzic A, Tournoux F, Cloutier G, Garcia D. A unified framework combining coherent compounding, harmonic imaging and angular coherence for simultaneous high-quality B-mode and tissue Doppler in ultrafast echocardiography. IEEE Trans Ultrason Ferroelectr Freq Control 2025; 72:141–52.

[34] Stanziola A, Toulemonde M, Li Y, Papadopoulou V, Corbett R, Duncan N, et al. Motion artifacts and correction in multipulse high-frame rate contrast-enhanced ultrasound. IEEE Trans Ultrason Ferroelectr Freq Control 2018;66:417–20.

[35] Cormier P, Porée J, Bourquin C, Provost J. Dynamic myocardial ultrasound localization angiography. IEEE Trans Med Imaging 2021;40:3379–88.

[36] Simpson DH, Chin CT, Burns PN. Pulse inversion Doppler: a new method for detecting nonlinear echoes from microbubble contrast agents. IEEE Trans Ultrason Ferroelectr Freq Control 1999;46:372–82.

[37] Shen CC, Chou YH, Li PC. Pulse inversion techniques in ultrasonic nonlinear imaging. J Med Ultrasound 2005;13:3–17.

[38] Tremblay-Darveau C, Williams R, Sheeran PS, Milot L, Bruce M, Burns PN. Concepts and tradeoffs in velocity estimation with plane-wave contrast-enhanced Doppler. IEEE Trans Ultrason Ferroelectr Freq Control 2016;63:1890–905.
[39] Kasai C, Namekawa K, Koyano A, Omoto R. Real-time two-dimensional blood flow imaging using an autocorrelation technique. IEEE Trans Son Ultrason 1985;32:458–64.
[40] Torp H. Clutter rejection filters in color flow imaging: a theoretical approach. IEEE Trans Ultrason Ferroelectr Freq Control 1997;44:417–24.
[41] Loupas T, Powers JT, Gill RW. An axial velocity estimator for ultrasound blood flow imaging, based on a full evaluation of the Doppler equation by means of a two-dimensional autocorrelation approach. IEEE Trans Ultrason Ferroelectr Freq Control 1995;42:672–88.